Available online at www.sciencedirect.com
ScienceDirect
Trans. Nonferrous Met. Soc. China 30(2020) 2339−2354
Transactions of Nonferrous Metals Society of China
www.tnmsc.cn

Process−microstructure−properties relationship in Al−CNTs−Al_2O_3 nanocomposites manufactured by hybrid powder metallurgy and microwave sintering process

Meysam TOOZANDEHJANI[1], Farhad OSTOVAN[2], Khairur Rijal JAMALUDIN[1], Astuty AMRIN[1], Khamirul Amin MATORI[3], Ehsan SHAFIEI[2]

1. Razak Faculty of Technology and Informatics, Universiti Teknologi Malaysia Kuala Lumpur, 54100 Jalan Semarak, Kuala Lumpur, Malaysia;
2. Department of Material Science and Engineering, Islamic Azad University, Bandar Abbas Branch, Bandar Abbas, Hormozgan, Iran;
3. Department of Physics, Faculty of Science, Universiti Putra Malaysia, 43400, Serdang, Selangor, Malaysia

Received 25 December 2019; accepted 3 June 2020

Abstract: Al−2CNTs−$x$$Al_2O_3$ nanocomposites were manufactured by a hybrid powder metallurgy and microwave sintering process. The correlation between process-induced microstructural features and the material properties including physical and mechanical properties as well as ultrasonic parameters was measured. It was found that physical properties including densification and physical dimensional changes were closely associated with the morphology and particle size of nanocomposite powders. The maximum density was obtained by extensive particle refinement at milling time longer than 8 h and Al_2O_3 content of 10 wt.%. Mechanical properties were controlled by Al_2O_3 content, dispersion of nano reinforcements and grain size. The optimum hardness and strength properties were achieved through incorporation of 10 wt.% Al_2O_3 and homogenous dispersion of CNTs and Al_2O_3 nanoparticles (NPs) at 12 h of milling which resulted in the formation of high density of dislocations and extensive grain size refinement. Also both longitudinal and shear velocities and attenuation increase linearly by increasing Al_2O_3 content and milling time. The variation of ultrasonic velocity and attenuation was attributed to the degree of dispersion of CNTs and Al_2O_3 and also less inter-particle spacing in the matrix. The larger Al_2O_3 content and more homogenous dispersion of CNTs and Al_2O_3 NPs at longer milling time exerted higher velocity and attenuation of ultrasonic wave.

Key words: hybrid composite; aluminum composites; powder metallurgy; microwave sintering; microstructure; mechanical properties; ultrasonic velocity; ultrasonic attenuation

1 Introduction

Aluminium matrix composites (AMCs) have been developed by the incorporation of various reinforcements into aluminium (Al) matrix and extensively investigated [1−4]. Hybrid AMCs are the latest generation of AMCs which provide the higher level of mechanical properties and excellent performances since they combine the individual properties of each constituent [5]. Hybrid AMCs exhibit excellent tensile and compression strength, elastic modulus, fatigue strength and wear and creep resistance as compared to single-reinforced composites [4−8]. In a very recent study, CHEN et al [8] have reported extraordinary reinforcing effect of Al/CNTs composites in the presence of in-situ Al_2O_3 nanoparticles (NPs). Interestingly, they reported the enhancement of ductility comparable to the high-strength AA7075-T6 alloy knowing that Al/CNTs have a low ductility (≤5%).

The properties of hybrid AMCs can be tailored

Corresponding author: Farhad OSTOVAN; Tel: +98-9131124117; E-mail: F.ostovan@gmail.com
DOI: 10.1016/S1003-6326(20)65383-3

by varying the type, size and amount of reinforcements. Most particle reinforcement materials used in AMCs are ceramics such as oxides, carbides, and nitrides which have been used in different types, shapes, and sizes. They are characterized by their high strength and stiffness both at ambient and elevated temperatures [3]. Among ceramic reinforcements, alumina (Al_2O_3) is one of the most widely used ones due to high availability, low cost and overall good properties [3]. Regarding fibrous materials, carbon nanotubes (CNTs) have been recently used in a wide variety of industries to produce novel AMCs owing a high strength and elasticity modulus [8−11]. However, in order to get the benefits of these small and high strength reinforcement phases, a uniform dispersion of those reinforcements throughout Al matrix is required. To reach this goal, depending on the type of reinforcement, different processing techniques including liquid state and solid-state manufacturing can be used. Different processing and finishing techniques and their corresponding parameters also provide various characteristic profiles while the similar chemical compositions are used. In the interest of authors, ball milling combined with powder metallurgy is an effective method for homogeneous dispersion of a wide variety of nanoparticles [12−15].

In earlier researches, single-reinforced pure Al-CNTs and Al−Al_2O_3 nanocomposites have been successfully synthesized using ball milling and powder metallurgy route technique [12,15−18]. The synthesized single-reinforced Al-CNTs and Al−Al_2O_3 nanocomposites showed enhanced microhardness, compression strength, and elastic modulus as compared to pure Al owing to dispersed individual CNTs and Al_2O_3 NPs. However, enhancing the mechanical properties was found to be more profound in the presence of CNTs except for mass fraction more than 2 wt.%. This was due to the fact that the mechanical properties of Al−CNTs and Al−Al_2O_3 are decided by the microstructure of the material mainly dispersion uniformity of CNTs and Al_2O_3 NPs. In this work, 2 wt.% CNTs were added to Al matrix along with Al_2O_3 NPs as a mixing agent in order to develop hybrid Al−CNTs−Al_2O_3 nanocomposites. Al−CNTs−Al_2O_3 nanocomposite powders were processed using a ball milling technique and consolidated in a microwave sintering assisted powder metallurgy route. Finally, a comprehensive morphological, microstructural and mechanical as well as non-destructive characterization was performed to reveal the process−microstructure−properties relationship in hybrid Al−CNTs−Al_2O_3 nanocomposites.

2 Experimental

Al powder (Merck KGaA), α-Al_2O_3 (Sigma Aldrich) and CNTs (Cheap Tubes) powders were used as raw materials. The characteristics of the powder materials used in this study are presented in Table 1.

Table 1 Characteristics of raw materials used in this research

Material	Shape	Mean diameter/ nm	Mean length/ nm	Density/ ($g \cdot cm^{-3}$)
Aluminum	Flake	−	−	2.70
CNTs	Multi-walled	20−30	10−30	2.10
α-Al_2O_3	Spherical	200	−	3.95

Initially, CNTs and Al_2O_3 NPs were mixed using ultrasonication technique in two different steps to ensure good dispersion of both NPs. First, 0.4 g of CNTs (as 2 wt.% in the nanocomposite matrix) was scaled and dispersed into 100 mL of acetone using a probe-type ultrasonicator (200 W). Ultrasonication was performed at a speed of 600 r/min for 0.5 h at room temperature. Acetone was used as the solvent for dispersion of NPs as reported by ROSELINE and PARAMASIVAM [19]. The large vibrations induced by ultrasonication assist separation of CNTs and avoided agglomeration of CNTs. Certain amounts of Al_2O_3 NPs (0.2, 0.4, 1 and 2 g) were added to CNTs suspension where each of them was used as 1, 2, 5 and 10 wt.% of nanocomposite matrices. The dual-reinforcement slurry was ultrasonicated up to 3 h depending on the mass fraction used to obtain a uniform dispersion of Al_2O_3 NPs. Afterwards, each of the dual-reinforcement suspensions was drop-wise added to separate batches of pure Al powders which were mixed in acetone and separately ultrasonicated for 2 h until a uniform dispersion of nanocomposite particles was obtained. The as-synthesized powders were filtered using Whatman filter paper. The filtered powders were

then dried in vacuum oven at 60 °C for 480 min to ensure removal of the acetone.

As-synthesised nanocomposite powders were transferred to a ball milling jar and subjected to ball milling. Each of the obtained nanocomposite powders were ball-milled for 12 h, from which the optimum milling time was determined. Then, different series of hybrid Al−2CNTs−$x$$Al_2O_3$ were ball-milled in constant milling time of 8 h to separately investigate the effect of Al_2O_3 content. The ball milling procedure was tried to follow the similar procedure that authors used for synthesizing Al−CNTs and Al−Al_2O_3 nanocomposites [12,15−18]. The ball milling parameters and conditions are listed in Table 2. Finally, hybrid Al−2CNTs−$x$$Al_2O_3$ nanocomposite powders were obtained with 2 wt.% CNTs and 1, 2, 5 and 10 wt.% Al_2O_3 into pure Al matrix. Constant 2 wt.% of CNTs was added to the Al matrix which was decided based on the previous observations [12,18].

Nanocomposite powders were consolidated in a powder metallurgy route. Nanocomposite powders were then cold-pressed uniaxially at a pressure of 150 MPa using hydraulic pressing machine (ARMSTRONG, 15 t). In post-compaction stage, the green nanocomposite specimens were sintered in an assembled microwave furnace with frequency of 2.45 GHz and maximum power output of 900 W. Initially, the green compacts were subjected to 400 °C for 0.5 h for elimination of residual additives. The temperature was raised at a rate of 18 °C/min. Microwave sintering process was conducted at temperature of 530 °C for a soaking time of 45 min under high purity argon atmosphere (99.99%). Finally, the sintered specimens were cooled down to ambient temperature in the air.

Before the microstructural observation, the specimens underwent a standard metallographic procedure: grinding up to 2000 grit followed by polishing using 6 and 1 μm diamond pastes on 3 μm MD-Mol Nap. The morphology and dispersion uniformity of CNTs and Al_2O_3 NPs during ball milling were observed via SEM (Hitachi S−3400, Tokyo, Japan) and HRTEM (Tecnai G^2 20 S-TWIN), respectively. The fracture surface after compression test was examined using FESEM (7600F, JEOL Tokyo, Japan). The grain structure of specimens was characterized through electron backscatter diffraction (EBSD) using FESEM (JEOL 7600F) equipped with ATEX software. For EBSD observation, specimens were subjected to an additional finishing polishing by nano-diamond suspension using the VibroMet® 2 Vibratory polisher for 12 h. Specimens were kept in a vacuum chamber for 24 h before EBSD observation. MasterSizer analyzer (Malvern Instruments Ltd., Worcestershire, UK) was used to measure the particle size of nanocomposite powders. A Shimadzu X-ray detector (XRD−6000 diffractometer, Shimadzu Corporation, Osaka, Japan) was used to obtain the X-ray diffraction patterns of the nanocomposite powders after the milling process. The XRD diffractometer was operated with a Cu K_α radiation (λ=0.1542 nm) at 40 kV and 120 mA in the 2θ range of 20°−80°. Raman spectra of nanocomposite specimens were recorded using WITec (Alpha 300R) spectrometer with an excitation wavelength of 532 nm.

The apparent density of powders and bulk density were measured according to the ASTM B417−13 [20] and Archimedes method, respectively. The detail of bulk density measurement can be found elsewhere [16]. The theoretical density values of Al−CNTs−$x$$Al_2O_3$ nanocomposites were calculated by the rule of mixture. Pore volume fraction (φ) was determined as

$$\varphi = 1 - \frac{\rho}{\rho_0} \tag{1}$$

where ρ and ρ_0 represent the bulk density and the theoretical density of nanocomposites, respectively. The physical dimensional changes (PDC) or expansion of the nanocomposite specimens were determined according to the ASTM B610−13 [21] as follows:

$$\mathrm{PDC} = [(D_s - D_g)/D_g] \times 100\% \tag{2}$$

where D_g and D_s are the dimensions of the

Table 2 Ball milling parameters and conditions used for preparation of Al−2CNTs−$x$$Al_2O_3$ nanocomposite powders (BPR: mass ratio of ball to powder)

Rotational speed/(r·min^{-1})	BPR	Milling time/h	Ball (jar) material	Ball milling condition	Atmosphere
300	10:1	0.5−12	Tungsten carbide	Dry	Argon

specimens before and after sintering, respectively.

The micro-hardness (HV), nano-hardness (HN) and elastic modulus (E) measurements were performed using Micro Materials Nanotest™ indenter. During nanoindentation measurements, a load of 50 μN with dwell time of 5 s was applied using a standard Berkovich geometry tip in a 4×5 square pattern while the spacing between indents was 10 μm. HN, HV and E values were calculated according to the Oliver–Pharr method [22] and the average of total 20 indents was reported. The detail of measurements can be found elsewhere [18]. Compression test specimens were prepared according to the ASTM E9−89α. The tests were conducted at the ambient temperature by using a 15 kN INSTRON 3366 testing machine at a constant crosshead speed of 0.01 mm/min. The dimensions of cylindrical test coupon were 5 mm × 10 mm (D×L), where L/D ratio was 2. For compression test, three specimens were tested and the average values were reported.

Non-destructive ultrasonic testing was carried using a commercially available ultrasonic testing (UT) system consisting of an ultrasonic oscilloscope (Agilent, 100MHz), an ultrasonic pulser/receiver (RAM−5000, RITEC SNAP, USA) and transducers (X-cut and y-cut; Krautkramer). Ultrasonic measurements were conducted using the direct contact method between transducer and specimens in a pulse-echo configuration. Normal contact transducers of 2 and 4 MHz of both longitudinal and shear wave transducers were used to acquire the signals. Sonagel-W (T-09) was used as a couplant to provide effective contact between transducers and specimen surfaces. Experimental variables were kept constant during the signal capturing so that, applied identical conditions during ultrasonic measurements. Longitudinal and shear wave velocities (V) were calculated from the amplitude and position quantification of the 2nd and 3rd back-wall echoes obtained according to the following equation:

$$V = 2T / t \tag{3}$$

where T and t are the transition time or time of flight (TOF) between the two consecutive back-wall echos and thickness of the specimens, respectively.

The thickness of specimens was measured at the same signal acquisition points by a micrometer with the accuracy of ±0.01 mm. The average of three measurements at different signal acquisition points was obtained and the mean value was reported. The absolute accuracy in the velocity measurement was ±10 m/s, and the relative error was typically less than 10%. Attenuation coefficient (α) in pulse-echo technique was calculated by

$$\alpha = \frac{20\lg(A_1 / A_2)}{2d} \tag{4}$$

where A_1 and A_2 are the amplitude of the 2nd and 3rd back-wall echoes, and d is the thickness of the specimen in mm. The average of three measurements at three different signal acquisitions was obtained and the mean value was reported. The accuracy of attenuation measurements was ±8 dB/mm.

3 Results and discussion

3.1 Physical properties of hybrid Al−CNTs−Al_2O_3 nanocomposites

The variations of theoretical density, experimental density and porosity of sintered Al−2CNTs−$x$$Al_2O_3$ nanocomposites as a function of Al_2O_3 content are shown in Fig. 1(a). It can be seen

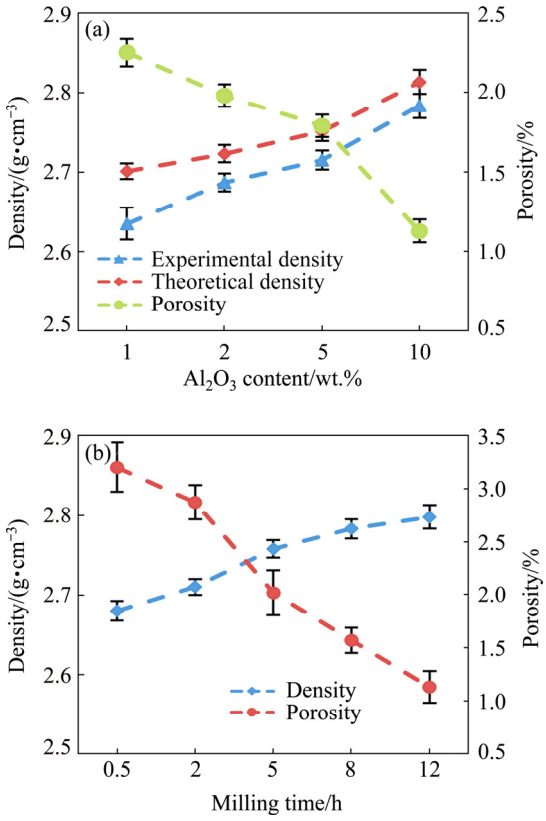

Fig. 1 Variations of density and porosity in Al−2CNTs−$x$$Al_2O_3$ nanocomposites at constant milling time of 8 h (a) and variations of experimental density and porosity in Al−2CNTs−5Al_2O_3 nanocomposite with milling time (b)

that both theoretical and experimental densities increase with increasing Al_2O_3 content. Theoretical density values of Al−2CNTs−$x$$Al_2O_3$ nanocomposites increase from 2.70 to 2.81 g/cm^3 by increasing Al_2O_3 content from 1 to 10 wt.%. Experimental density also shows a similar trend as observed in theoretical density. The increase of density is due to the fact that larger contents of Al_2O_3 NPs and/or the CNTs−Al_2O_3 clusters fill up the interstices between the Al particles as reported by RAZAVI HESABI et al [23]. The values of experimental density are lower than those of theoretical density, indicating the presence of porosities in the sintered specimens. However, the amount of porosity of Al−2CNT−$x$$Al_2O_3$ nanocomposites decreases with increasing Al_2O_3 content in an opposite manner of density.

Figure 1(b) shows the variations of density and porosity of sintered Al−2CNTs−5Al_2O_3 as a function of milling time. It can be seen that by increasing milling time, experimental density values increase while porosity values decrease. A similar trend was found in each of Al−2CNTs−$x$$Al_2O_3$ nanocomposites. The variation of density in MMCs during milling process depends on the morphology of the powders after milling, dispersion uniformity of reinforcements within the matrix, as well as the compaction and sintering parameters [16,24]. Since the compaction and sintering parameters were kept identical for all series of nanocomposites, the effect of compaction and sintering effect can be ignored here. The lower density values and larger amount of porosities of Al−2CNTs−$x$$Al_2O_3$ nanocomposites at the early stage of milling up to 2 h are due to the larger particle size, agglomeration of Al particle as well as clustering of CNTs and Al_2O_3 NPs as can be seen in the microstructure of Al−2CNTs−$x$$Al_2O_3$ nanocomposites (Fig. 2). These microstructural features interrupt the densification process and slow

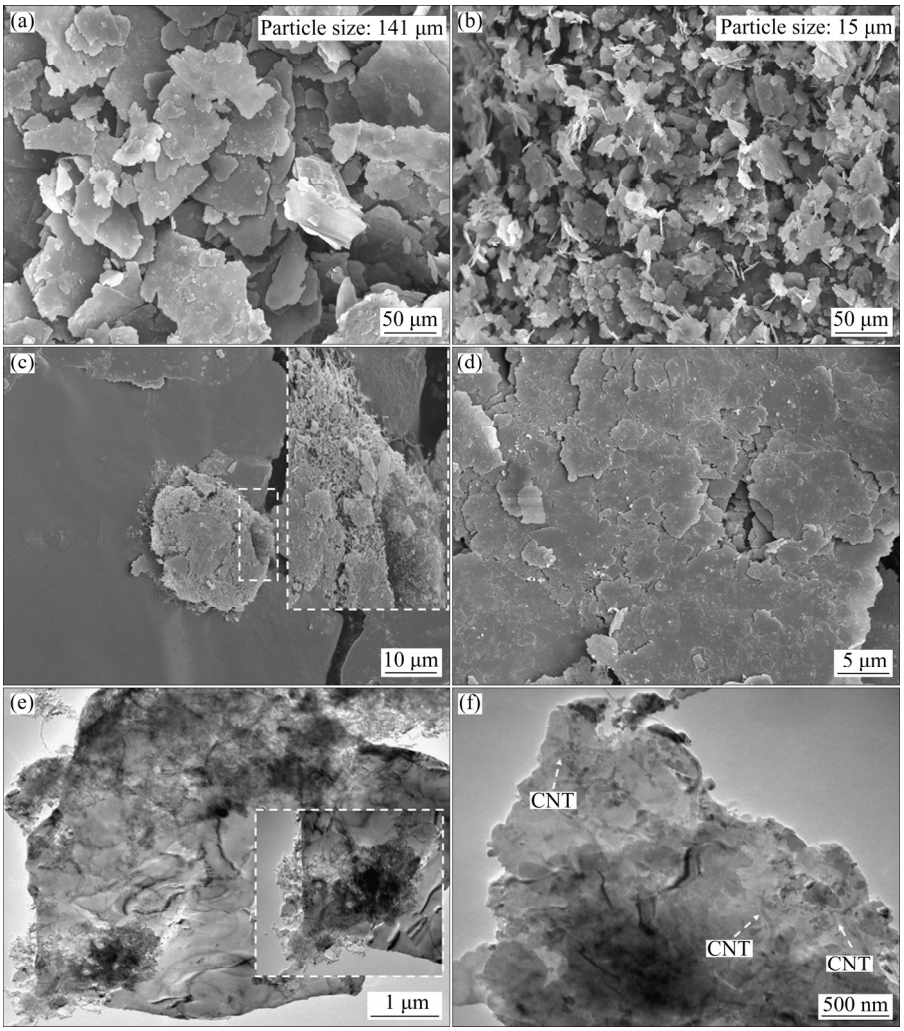

Fig. 2 Morphology and microstructural features of Al−2CNTs−5Al_2O_3 nanocomposite powders after 0.5 h (a, c, e) and 8 h (b, d, f) of ball milling

down the sintering process. In contrast, higher density values at longer milling time than 5 h are attributed to more homogenous dispersion of CNTs and Al_2O_3 NPs within Al matrix along with refined particle sizes which facilitate bonding of particles during sintering. Homogeneous dispersion of CNTs and Al_2O_3 NPs provides a small inter-particle space and tighter interfacial bonding between Al matrix and NPs resulting in denser sintered nanocomposites with less amount of debonding or cracks and porosities. In addition, a larger content of Al_2O_3 further refines the particle size of Al−2CNTs−$x$$Al_2O_3$, leading to the increment of density.

Figure 2 demonstrates the morphological and microstructural variations of Al−2CNTs−5Al_2O_3 nanocomposite powders with proceeding of milling process. First of all, initial flake-shape Al particles experience significant deformation in the vicinity of CNTs and Al_2O_3 NPs under high impact collision of the balls during milling process. The morphologies of Al−2CNTs−5Al_2O_3 nanocomposite powders after 0.5 and 8 h of milling are shown in Figs. 2(a) and (b), respectively. The fracturing of nanocomposite particles is the predominant mechanism during milling through which the mean particle size progressively decreases from 141 μm at the beginning of milling to 15 μm after 8 h of milling. Al−2CNTs−5Al_2O_3 nanocomposite reaches steady state after 5 h of milling and the morphology of nanocomposite particles stabilizes. It is also worth mentioning that almost no agglomeration of Al particles was found even at short milling time. The average particle size of powders further decreases with increasing Al_2O_3 content due to intensified fracturing of particles. At constant milling of 8 h, for example, Al−2CNTs−10Al_2O_3 nanocomposite had the lowest particle size of 10.82 μm compared with that of Al−2CNTs−1Al_2O_3 nanocomposite (37.67 μm) and Al−2CNTs−2Al_2O_3 nanocomposite (29.23 μm).

The progressive decrease in particle size exerts a more uniform dispersion of CNTs and Al_2O_3 NPs during milling. The FESEM micrographs in Figs. 2(c) and (d) show the dispersion uniformity of CNTs and Al_2O_3 NPs after 0.5 and 8 h of milling, respectively. At short milling time of 0.5 h, it can be seen that CNTs and Al_2O_3 NPs appear independently in large CNTs−Al_2O_3 clusters. TEM micrograph also reveals that some CNTs are entangled in the regions populated with Al_2O_3 NPs (Fig. 2(e)). After 8 h of milling, as it is expected, the dispersion uniformity of CNTs and Al_2O_3 NPs improves and a well-homogeneous dispersion is obtained. Al_2O_3 NPs are homogeneously dispersed within Al particles while most CNTs are embedded, which cannot be seen in Fig. 2(f). A similar trend can be found in each Al−2CNTs−$x$$Al_2O_3$ nanocomposite.

In line with density, the densification behaviour in Al−2CNTs−$x$$Al_2O_3$ nanocomposites is also improved with increasing Al_2O_3 content and milling time as shown in Table 3 and Fig. 3. It can be seen from Table 3 that Al−2CNTs−10Al_2O_3 nanocomposite has the highest densification of 98.4% owing to the better packing properties of powders due to extreme particle refining. Under the same compaction condition, smaller sizes of particles facilitate the densification of nanocomposite powders as compared to the larger particles [16]. The densification behaviour of Al−2CNTs−xAl_2O_3 nanocomposites varies in the same manner as in the apparent density which corresponds to the powder morphology and particle size of powders. The physical dimensional changes (PDC) of Al−2CNTs−$x$$Al_2O_3$ nanocomposites are more profound in the presence of larger Al_2O_3 contents. In powder metallurgy, the physical dimensional changes (PDC) or expansion is an observation of the grain growth during sintering process. It can be seen that with increasing the Al_2O_3 content, PDC values of nanocomposites increase from 1.67% to 2.22%. A positive PDC value indicates growth of the specimens, and a negative PDC value reflects shrinkage of the specimens. Dimensional changes of composites are highly dependent on the physical properties of the initial powders and the homogeneity of the

Table 3 Variations of apparent density, densification and physical dimensional changes in Al−2CNTs−$x$$Al_2O_3$ nanocomposites as function of Al_2O_3 content at constant milling time of 8 h

Nanocomposite system	Apparent density/ ($g\cdot cm^{-3}$)	Densification/ %	PDC/ %
Al−2CNTs−1Al_2O_3	1.49	94.2	1.67
Al−2CNTs−2Al_2O_3	1.54	95.2	1.87
Al−2CNTs−5Al_2O_3	1.66	97.7	2.10
Al−2CNTs−10Al_2O_3	1.77	98.4	2.22

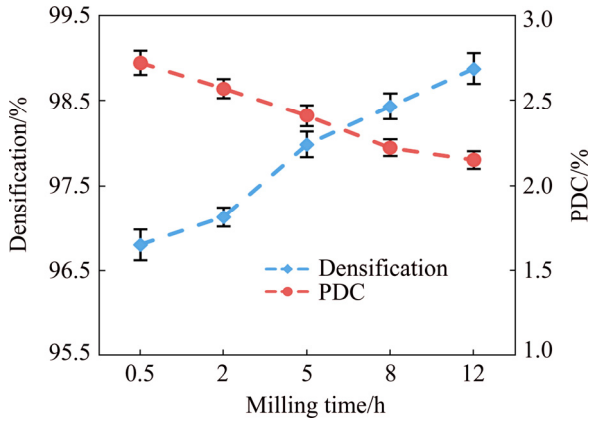

Fig. 3 Variations of densification and physical dimensional changes in Al−2CNTs−10Al_2O_3 nanocomposites as function of milling time

reinforcement particles along with compaction pressure, time and temperature of sintering [25].

Figure 3 shows the variations of densification and the physical dimensional changes in Al−2CNTs−10Al_2O_3 nanocomposite as a function of milling time. During milling of Al−2CNTs−10Al_2O_3 powders, particles are continuously fractured and refined, which improves the compressibility properties of the powders. Besides, uniform dispersion of CNTs and Al_2O_3 having less inter-particle spacing within Al matrix at longer milling time results in the denser sintered nanocomposite. Uniform dispersion of CNTs and Al_2O_3 NPs decreases the amount of porosities, so that a denser part could be obtained.

The variations of dimensional changes in Al−2CNTs−10Al_2O_3 nanocomposites as a function of milling time are also shown in Fig. 3. Refined Al particles, homogenously dispersed CNTs and Al_2O_3 NPs at longer milling time and in the presence of larger Al_2O_3 content result in less dimensional changes of nanocomposite specimens during sintering process, indicating less grain growth during sintering. The results are in agreement with previous work done by RAZAVI TOUSI et al [26].

3.2 Mechanical properties of hybrid Al−CNTs−Al_2O_3 nanocomposites

The variations of micro-hardness (HV), nano-hardness (HN), elastic modulus (E) and compressive strength (CS) of Al−CNTs−$x$$Al_2O_3$ nanocomposites as functions of Al_2O_3 content and milling time are summarized in Table 4. At constant milling time of 8 h, it can be seen that HV and HN

Table 4 Variation of HV, HN, E and CS of Al−CNTs−$x$$Al_2O_3$ nanocomposites as function of Al_2O_3 content and milling time

Nanocomposite	Milling time/h	HV	HN/GPa	E/GPa	CS/MPa
Al−2CNTs−1Al_2O_3	0.5	63.0±7.1	0.69±0.15	37.2±1.8	547±7
	2	67.9±5.3	0.75±0.11	39.1±2.2	551±8
	5	73.4±4.7	0.80±0.10	42.9±3.3	565±8
	8	79.2±6.2	0.87±0.11	47.9±2.1	572±6
	12	93.1±3.0	0.92±0.09	50.2±1.3	580±9
Al−2CNTs−2Al_2O_3	0.5	71.4±6.5	0.71±0.12	40.5±2.0	556±7
	2	77.9±4.1	0.79±0.11	44.3±1.7	561±8
	5	83.8±2.2	0.87±0.12	49.2±2.1	568±5
	8	96.5±3.0	0.96±0.10	54.9±1.4	578±6
	12	99.1±3.9	1.02±0.08	57.9±0.9	592±3
Al−2CNTs−5Al_2O_3	0.5	81.1±4.6	0.80±0.10	44.1±1.4	570±2
	2	83.7±2.3	0.88±0.06	51.7±1.9	581±3
	5	96.2±4.2	0.98±0.04	58.6±1.1	599±2
	8	112.9±5.0	1.12±0.06	62.4±1.2	622±4
	12	121.7±3.1	1.22±0.03	68.0±1.2	651±4
Al−2CNTs−10Al_2O_3	0.5	96.1±5.0	1.03±0.06	61.2±1.3	598±2
	2	110.5±4.1	1.18±0.05	64.4±1.1	613±1
	5	125.5±3.3	1.33±0.07	71.3±0.7	643±2
	8	131.5±3.0	1.41±0.02	79.2±1.0	663±4
	12	142.2±1.6	1.49±0.02	86.4±0.8	678±3

values of Al−2CNTs−$x$$Al_2O_3$ nanocomposites increase with increasing Al_2O_3 content. HV values increase from HV 79.2 to a maximum of HV 131.5, representing 39% increase of HV with increasing Al_2O_3 content. HN increases by 38% with increasing Al_2O_3 content. Similarly, E and CS values of Al−2CNTs−$x$$Al_2O_3$ nanocomposites increase with increasing Al_2O_3 content. Al−2CNTs−$x$$Al_2O_3$ nanocomposites present higher hardness and strength than single-reinforced Al−CNTs and Al−Al_2O_3 nanocomposites just as reported at earlier works [12,15−18]. This can be attributed to the simultaneous presence of CNTs and Al_2O_3 NPs and larger induced deformation to the structure of nanocomposites.

The presence of homogeneous dispersed CNTs and Al_2O_3 NPs within the soft Al matrix enhances the mechanical properties as also reported in previous works [27,28]. Figure 4(a) shows the typical TEM image of the sintered Al−2CNTs−10Al_2O_3 nanocomposites which confirms the homogeneously dispersed CNTs and Al_2O_3 NPs. Less amount of CNTs can be seen in the TEM micrographs, which is associated with the embedding of the CNTs into Al matrix. The insert of Fig. 4(a) shows single-embedded CNTs in Al

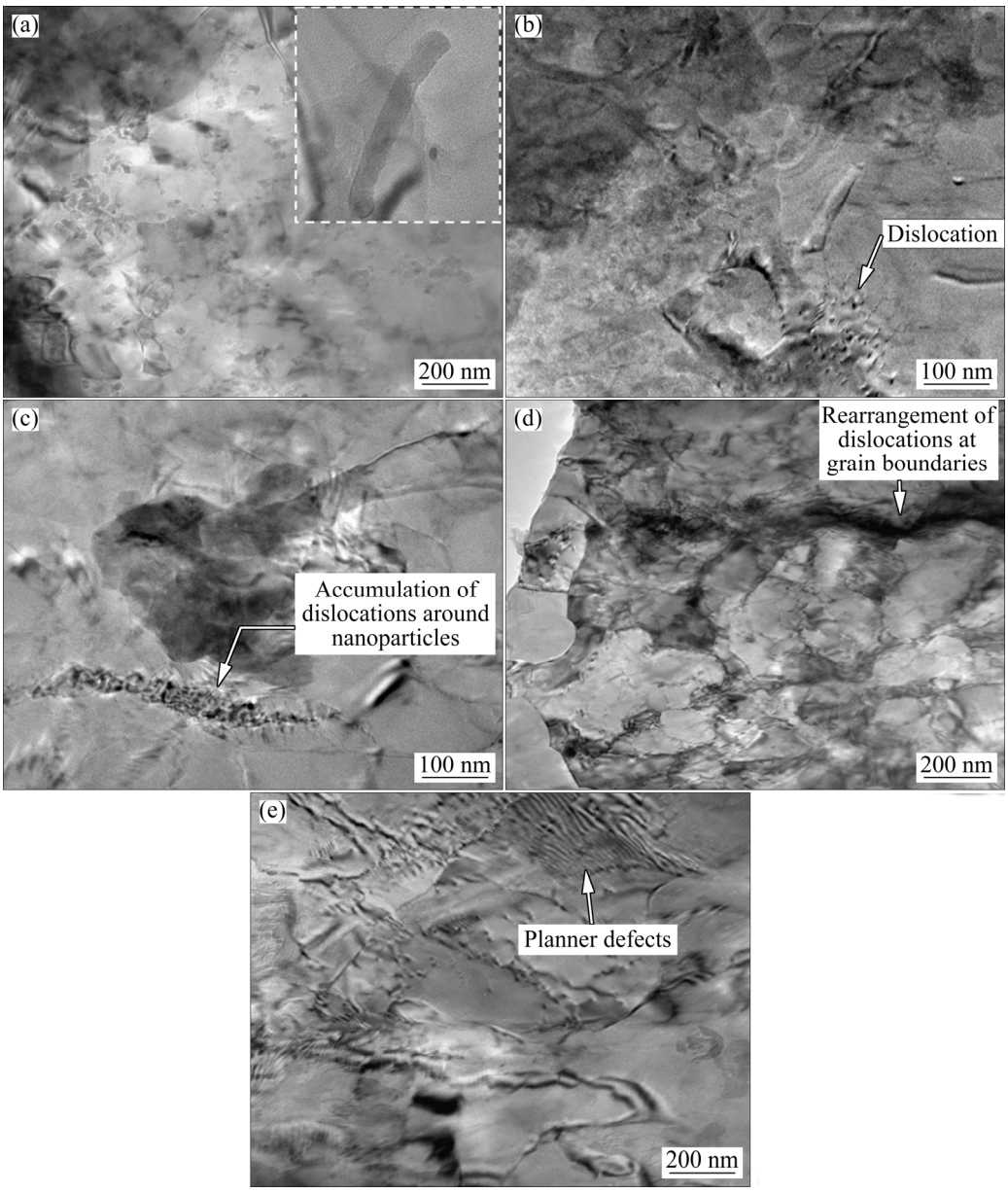

Fig. 4 HRTEM micrographs of Al−2CNTs−10Al_2O_3 nanocomposite showing dispersion uniformity of CNTs and Al_2O_3 nanoparticles (a), formation of dislocations (b, c), rearrangement of dislocations around grain boundaries (d) and planner defects (e)

matrix. The deformed and refined structure of nanocomposites generates high density dislocations and fine sub-grains during ball milling and consolidation process. High density of generated dislocation introduces severe strain hardening to the matrix powders and further hardens Al−2CNTs−$x$$Al_2O_3$ nanocomposites [16,17,29]. According to AKBARPOUR et al [27], dislocations are formed due to the thermal mismatch between the matrix and reinforcements for fulfilling geometrical conditions. Well dispersed and embedded CNTs and Al_2O_3 NPs at longer milling time having less inter-particle spacing obstruct deformation of ductile matrix, so a large amount of high-density dislocations are formed around the NPs as shown in Figs. 4(b) and (c). Moreover, it can also be seen that the presence of CNTs and Al_2O_3 NPs in Al matrix introduces planner defects to the microstructure (Fig. 4(e)).

According to FATHY et al [30], plastic deformation of Al grains during ball milling and consolidation leads to a coordinated deformation between adjacent grains and results in generation of more density of dislocations. Figure 4(d) shows the rearrangement of dislocations around grain boundaries and formation of sub-grains. When the density of dislocations reaches a critical limit, dislocations rearrange themselves to a lower energy state leading to the formation of sub-grains with low angle grain boundaries. Eventually, sub-grains turn into high-angle boundaries and become grains with near nano-scale sizes [31−33]. However, the grain refinement can happen as the result of the pinning effect of NPs during consolidation [27]. Figure 5 shows a typical surface morphology and grain structure in sintered Al−2CNTs−2Al_2O_3 nanocomposite. The grain size of nanocomposite is distributed in the nano range of about 28 nm (Fig. 5(b)).

Along with increase of the dislocation density, the crystalline size refinement and solid solution hardening resulting from severe plastic deformation within milling process are other reasons for hardening in Al−2CNTs−$x$$Al_2O_3$ nanocomposites. The crystalline size of Al−2CNTs−$x$$Al_2O_3$ nanocomposites were calculated according to the XRD patterns in Fig. 6(a). The crystalline size of Al−2CNTs−$x$$Al_2O_3$ nanocomposites decreases from 30.65 to 16.82 nm with increasing of Al_2O_3 content. In contrast, lattice strain increases from 0.30% to 0.71%. The main contribution to the decrement of crystalline size is the generation of dislocations as a result of accelerated work hardening and local plastic deformation owning to the interaction between hard CNTs and Al_2O_3 NPs and dislocations [34,35]. Generation of dislocations is accelerated with increasing Al_2O_3 content. Also, the interaction of larger content of CNTs and Al_2O_3 NPs with dislocations during milling further hinders the dislocation movement which leads to an increase in dislocation density and subsequently strain accumulation in particles. As a matter of fact, the final crystalline size of Al matrix is decided primarily by reinforcement content [16].

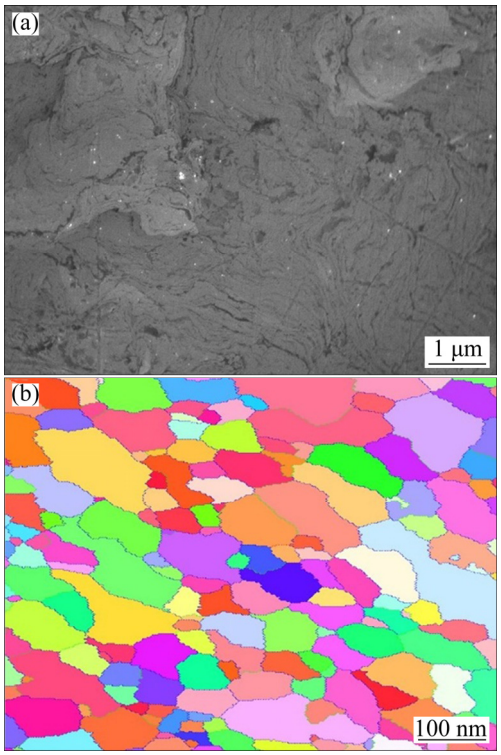

Fig. 5 Optical microscopy image (a) and EBSD micrograph (b) of Al−2CNTs−2Al_2O_3 nanocomposite

Another important feature in XRD diffraction patterns of Al−2CNTs−$x$$Al_2O_3$ is the occurrence of Al_4C_3 phase. Al_4C_3 phase is formed as a result of the interfacial reaction between the Al matrix and damaged CNTs or carbon atoms from amorphous carbon [36−38]. The probability of occurrence of Al_4C_3 phase increases by increasing Al_2O_3 content (Fig. 6(a)) as revealed by Raman spectra of CNTs. Figure 6(b) shows the Raman spectra of the as-received CNTs along with Al−2CNTs−1Al_2O_3 and Al−2CNTs−10Al_2O_3 nanocomposites which reveals the structural defects in CNTs during synthesizing

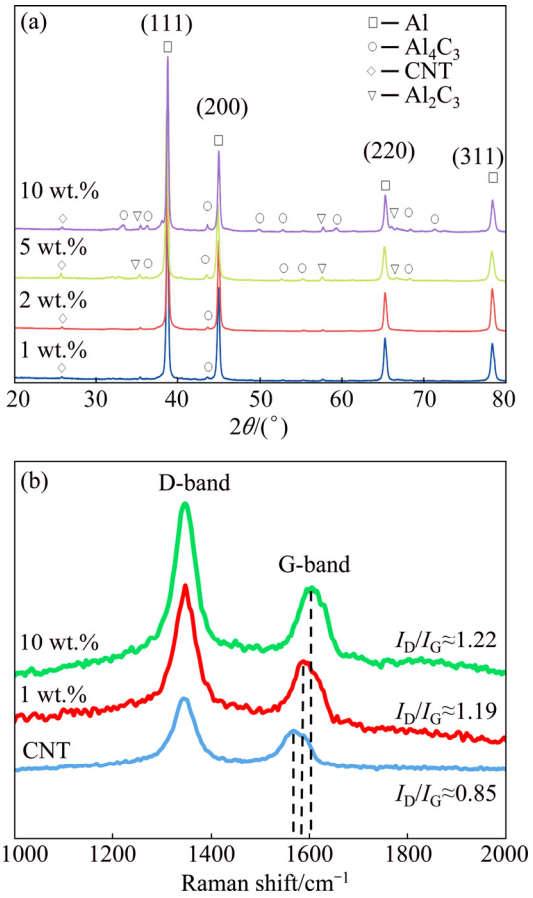

Fig. 6 XRD patterns (a) and Raman spectra (b) of Al−2CNTs−$x$$Al_2O_3$ nanocomposites as function of Al_2O_3 content at milling time of 8 h

procedure. It can be seen that I_D/I_G values increase from 0.88±0.05 in as-received CNTs to 1.19±0.03 and 1.22±0.01 in Al−2CNTs−1Al_2O_3 and Al−2CNTs−10Al_2O_3, respectively, corresponding to an increased proportion of disordered carbon. The HRTEM micrographs of Fig. 7 reveal the formation of Al_4C_3 and interfacial reaction between Al and CNTs in Al−2CNTs−10Al_2O_3 and Al−2CNTs−5Al_2O_3 nanocomposites.

The variations of mechanical properties of Al−2CNTs−$x$$Al_2O_3$ nanocomposite as a function of milling time are also presented in Table 4. HV and HN values of each Al−2CNTs−$x$$Al_2O_3$ nanocomposite increase with increasing milling time. A similar trend is found in the variation of E and CS with increasing milling time. Lower mechanical properties at shorter milling time are attributed to the large particle size of powders and heterogeneously dispersed CNTs and Al_2O_3 NPs, which results in poor sintering of these nanocomposites. The enhancement of mechanical properties at long milling time is due to more homogenous dispersion of CNTs and Al_2O_3 NPs within Al matrix along with effective grain refining of particles at longer milling time. Homogeneous dispersion of CNTs and Al_2O_3 decreases the inter-particle distances so that better bonding of particles and consequently enhanced strength properties could be achieved. Besides, it significantly reduces the amount of porosity and cracks presented in the sintered compacts and further improves the mechanical properties. It has been reported that porosities and cracks significantly reduce the measured elastic modulus of MMCs [39,40]. Clustering of CNTs−Al_2O_3 and porosities causes stress concentration and unexpected fracture thus, lower strength.

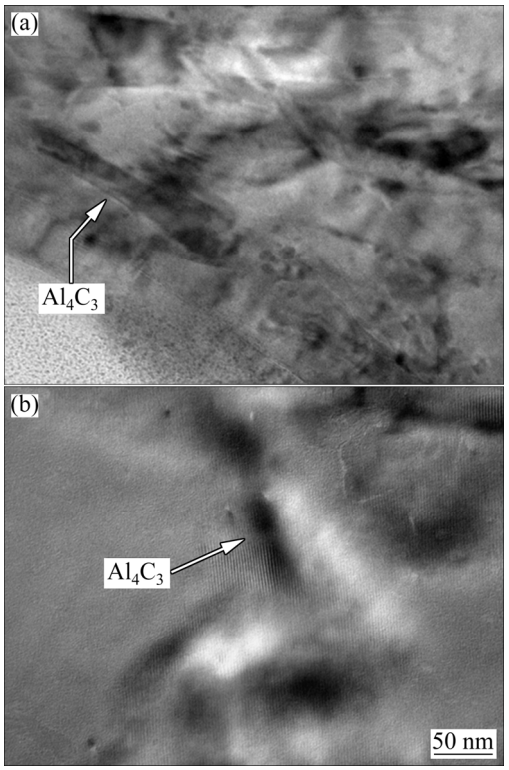

Fig. 7 HRTEM micrographs of Al−2CNTs−10Al_2O_3 (a) and Al−2CNTs−5Al_2O_3 (b) nanocomposites milled for 8 h showing formation of Al_4C_3

Typical fracture features of hybrid Al−CNTs−$x$$Al_2O_3$ nanocomposites under compression loading are shown in Fig. 8. The fracture is initiated from the location of voids and clustered CNTs−Al_2O_3 NPs (Fig. 8(a)). Figures 8(b) and (c) represent the fracture surface of those nanocomposites milled for shorter milling time. The agglomeration of CNTs−Al_2O_3 NPs provided sites for crack initiation and

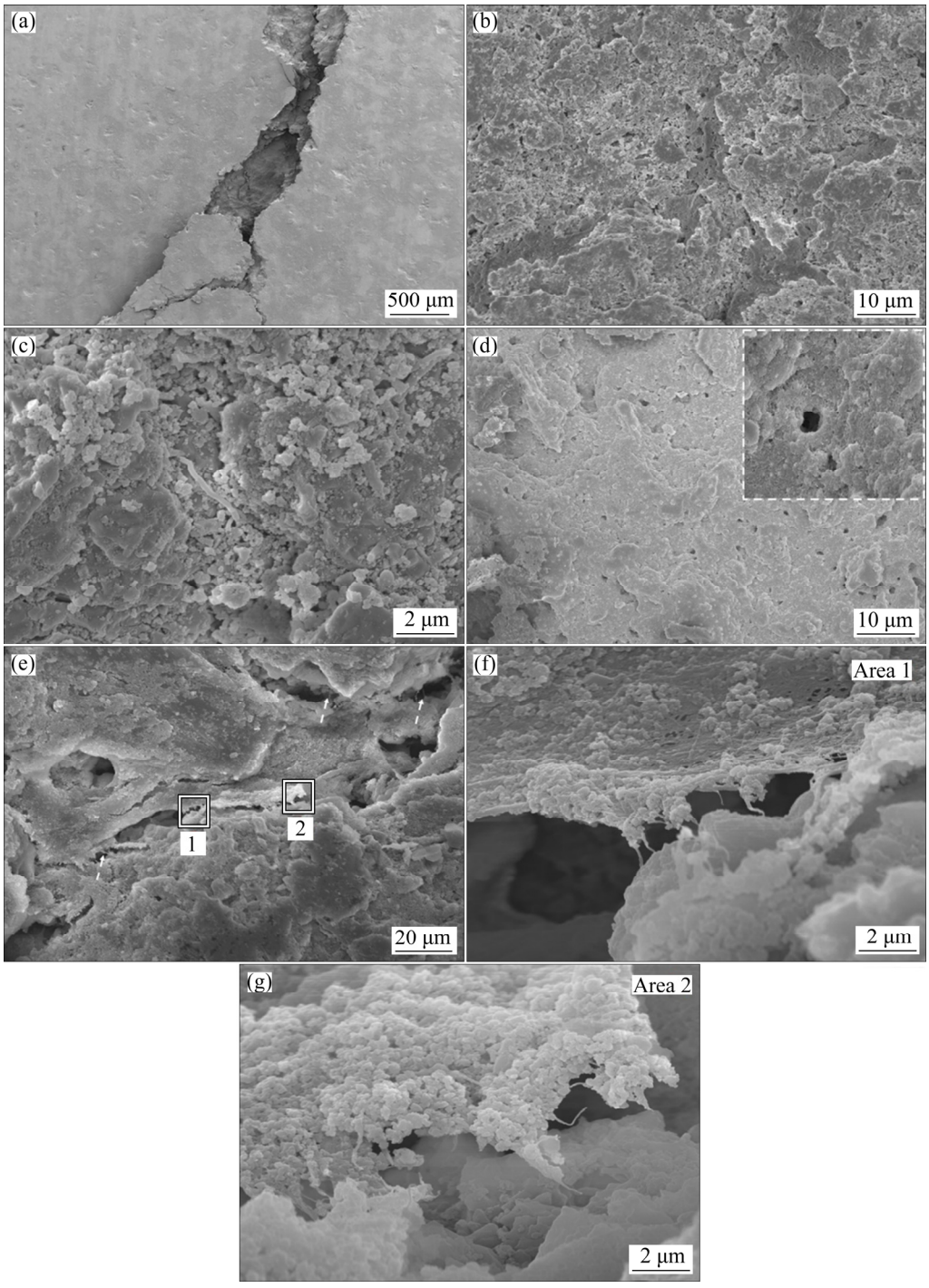

Fig. 8 Representative fracture surfaces of Al−CNTs−10Al_2O_3 nanocomposites at shorter milling time (a−c) and longer milling time (d−g)

acted as a stress concentration sites. According to CASATI and VEDANI [3], agglomerated regions and also the aggregation of oxide particles on the fracture surface may provide the sites for crack initiation, resulting in decrease in the ductility of composite. The fracture surfaces of those nanocomposites milled for longer milling time are represented in Figs. 8(d−g). Several pulled-out CNTs can be observed on the fracture surface, as marked by arrows in Fig. 8(e).

3.3 Ultrasonic properties of hybrid Al−CNTs−*x*Al_2O_3 nanocomposites

The variations of the longitudinal wave (V_l) and shear wave (V_s) velocities in Al−CNTs−*x*Al_2O_3 nanocomposites as functions of Al_2O_3 content and

milling time measured by 2 MHz and 4 MHz transducers are shown in Fig. 9. It can be seen that V_l values at both 2 and 4 MHz increase approximately linearly with increasing Al_2O_3 content (Fig. 9(a)). Velocity measurements taken by 2 and 4 MHz transducers are yielded identical results. A similar trend was found in the variation of V_s as a function of Al_2O_3 content (Fig. 9(b)). The increase in V_l and V_s velocities with increasing Al_2O_3 content can be explained by the interaction of the ultrasonic wave front with Al particles and dispersed NPs within the Al particles. Ultrasonic wave travels faster in CNTs and Al_2O_3 phase (stiffer phase) compared to Al matrix. Then, a larger Al_2O_3 content yields a higher ultrasonic velocity. In addition, the structural and microstructural variations associated with the addition of CNTs and Al_2O_3 NPs reflect as the increase of both V_l and

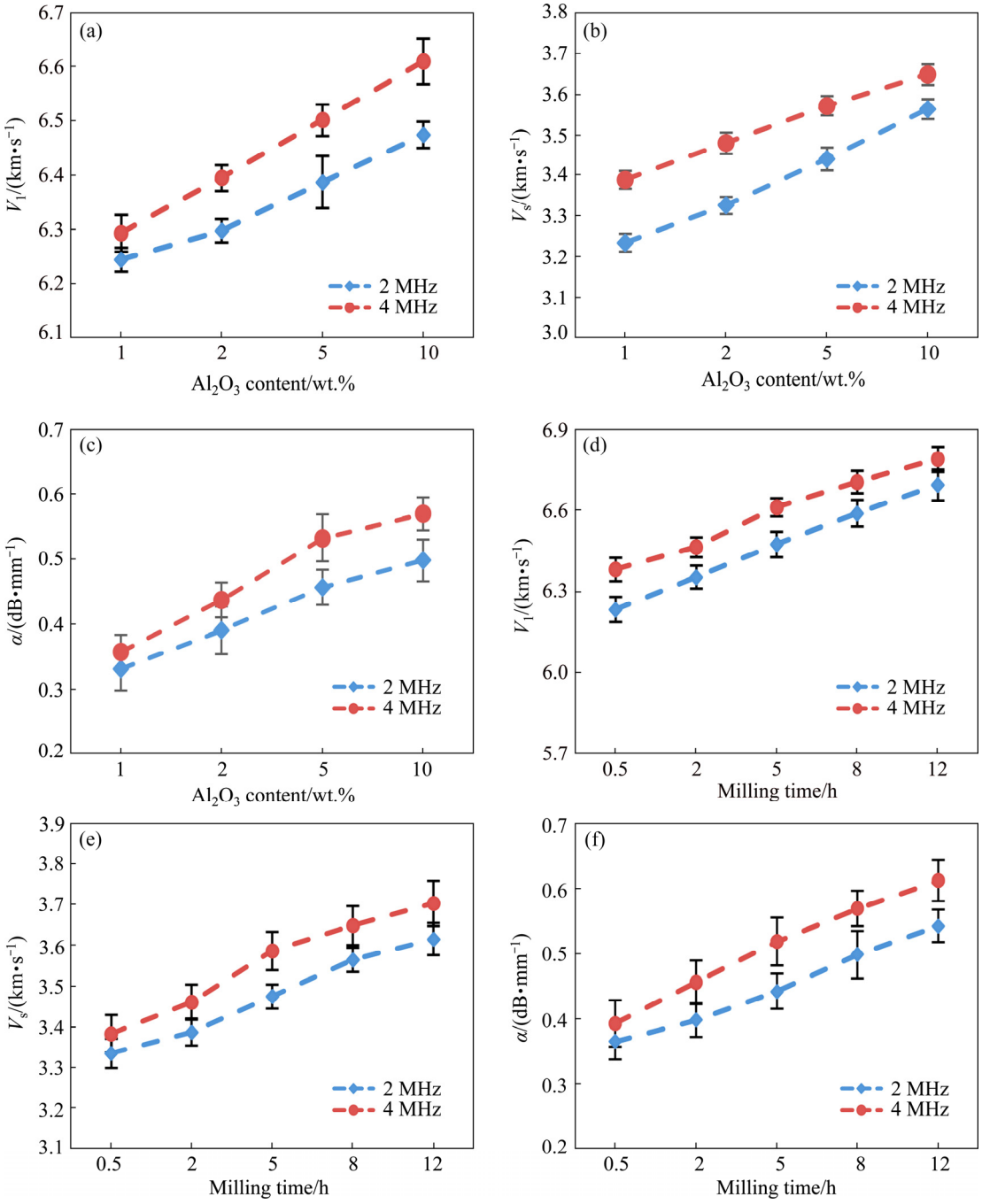

Fig. 9 Variations of longitudinal velocity, shear velocity and attenuation coefficient in Al−2CNTs−$x$$Al_2O_3$ nanocomposites as function of Al_2O_3 content (a−c) and those of Al−2CNTs−10Al_2O_3 nanocomposites as function of milling time (d−f)

V_s. Due to the difference between the elastic modulus of the soft Al matrix and hard CNTs and Al_2O_3, the increase in Al_2O_3 content results in the increase of the elastic modulus and in turn the ultrasonic velocity. The ultrasonic wave velocities are mainly determined by the difference between elastic moduli of material constituents [41].

The value of attenuation coefficient (α) also increases with increasing Al_2O_3 content in Al−2CNTs−$x$$Al_2O_3$ nanocomposites (Fig. 9(c)). The observed behaviour in α values is related to the presence of different amounts of dispersed CNTs and Al_2O_3 NPs in the microstructure. When an ultrasonic incident wave travels into the composite material, it will be largely attenuated at the interface between the matrix and reinforcement, where the two materials differ largely in their acoustic impedance. The magnitude of attenuation of ultrasonic wave is proportional to the number of scattering centres, i.e. particle−matrix interfaces [42]. Scattering of an ultrasonic wave depends on size, shape, type and volume fraction of the material components as reported by EL-DALY and HAMMAD [43] and EL-DALY et al [44]. Therefore, a large fraction of CNTs and Al_2O_3 NPs induce greater attenuation of ultrasonic incident wave, thereby resulting in higher values of attenuation coefficient. In addition, the presence of Al_4C_3 phases and crushed Al_2O_3 oxide layers which are presented as a dispersoid within microstructure as discussed earlier provides more scattering point and further increases the attenuation of ultrasonic wave.

The variations of V_l and V_s velocities in Al−2CNTs−10Al_2O_3 nanocomposites as a function of milling time are shown in Figs. 9(c) and (d). Both V_l and V_s velocities increase as milling time increases in a linear manner. Microstructural variations during ball milling of Al−2CNTs−10Al_2O_3 nanocomposites modify the ultrasonic properties. Homogenous dispersion of CNTs and Al_2O_3 within Al particles, reduction of inter-particle spacing, and particle size refinement contribute to the increase of elastic modulus and consequently V_l and V_s. In addition, homogeneous dispersion of CNTs and Al_2O_3 decreases the air gaps and porosity ratio between the constituents and provides a good bonding between the Al_2O_3 NPs and Al matrix. This increases ultrasonic velocities considerably as also reported by EL-DALY et al [45,46]. The heterogeneous dispersion of CNTs and Al_2O_3 and clusters of CNTs−Al_2O_3 which are deboned from the Al matrix is responsible for lower V_l and V_s at a shorter milling time.

Figure 9(f) shows the variation of α values of Al−2CNTs−10Al_2O_3 as a function of milling time. It can be seen that α values at both frequencies increase as the milling time increases. The homogeneous dispersion of CNTs and Al_2O_3 and reduced inter-particle spacing increase the probability of interaction of traveling ultrasonic waves with NPs and Al matrix lying around, resulting in increasing the attenuation of ultrasonic waves. In contrast, the heterogeneous dispersion of CNT and Al_2O_3 nanoparticle and the presence of Al_2O_3 clusters cause the uniformity of acoustic attenuations at different locations of the same specimen as reported by WU et al [47].

4 Conclusions

(1) Ball milling procedure along with ultrasonication exerts extensive particle refining, homogeneous dispersion of CNTs and Al_2O_3 NPs into Al matrix. Particle size of Al−CNTs−Al_2O_3 nanocomposites decreases by prolonging the milling process and results in homogeneous dispersion of CNTs and Al_2O_3 NPs. These microstructural variations are accelerated in the presence of large Al_2O_3 contents.

(2) The physical properties are closely associated with the powder characteristics including morphology and size of the powders after ultrasonication and ball milling. Density and densification of hybrid Al−CNTs−Al_2O_3 nanocomposites are improved due to particle refining at longer milling time and larger Al_2O_3 contents as well as less amount of porosities.

(3) The mechanical properties of Al−CNTs−Al_2O_3 nanocomposites are enhanced in the presence of larger Al_2O_3 contents and increase in the milling time. Enhancement of mechanical properties can be achieved by the incorporation of larger Al_2O_3 content, good dispersion of CNTs and Al_2O_3 NPs, formation of a high density of dislocations along with extensive grain size refinement.

(4) Both longitudinal and shear velocities and attenuation increase linearly by increasing Al_2O_3 contents and milling time. The variations in ultrasonic wave velocities are directly associated

with homogeneous dispersion of both CNTs and Al_2O_3 NPs, less inter-particle spacing which contributes to improved elastic modulus of nanocomposites and in turn ultrasonic velocities, large weight fraction of Al_2O_3 NPs induces greater attenuation of ultrasonic incident wave, thereby resulting in higher values of attenuation coefficient.

Acknowledgments

The authors gratefully acknowledge the financial support from the Professional Development Research University grant (No. 04E36). The authors also thank Dr. Md Shuhazlly Mamat and Prof. Sidek Abdul Aziz for their support.

References

[1] KAINER K U. Metal matrix composites: Custom-made materials for automotive and aerospace engineering [M]. Weinheim, Germany: Wiley-VCH, 2006.

[2] ROHATGI P, SCHULTZ B. Light weight metal matrix composites-stretching the boundaries of metals [J]. Materials Letters, 2007, 2: 6−9.

[3] CASATI R, VEDANI M. Metal matrix composites reinforced by nanoparticles—A review [J]. Metals, 2014, 4: 65−83.

[4] UJAH C O, POPOOLA P, POPOOLA O, AIGBODION V, OLADIJO P. Improving tribological and thermal properties of Al alloy using CNTs and Nb nanopowder via SPS for power transmission conductor [J]. Transactions of Nonferrous Metals Society of China, 2020, 30: 333−343.

[5] ROUHI M, MOAZAMI-GOUDARZI M, ARDESTANI M. Comparison of effect of SiC and MoS_2 on wear behavior of Al matrix composites [J]. Transactions of Nonferrous Metals Society of China, 2019, 29: 1169−1183.

[6] SHARMA A, SHARMA V M, PAULA J. A comparative study on microstructural evolution and surface properties of graphene/CNT reinforced Al6061−SiC hybrid surface composite fabricated via friction stir processing [J]. Transactions of Nonferrous Metals Society of China, 2019, 29: 2005−2026.

[7] OSTOVAN F, AMANOLLAH S, TOOZANDEHJANI M, SHAFIEI E. Fabrication of Al5083 surface hybrid nanocomposite reinforced by CNTs and Al_2O_3 nanoparticles using friction stir processing [J]. Journal of Composite Materials, 2020, 54: 1107−1117.

[8] CHEN B, KONDOH K, LI J S, QIAN M. Extraordinary reinforcing effect of carbon nanotubes in aluminium matrix composites assisted by in-situ alumina nanoparticles [J]. Composites B, 2020, 183: 107691.

[9] CHEN B, SHEN J, YE X, JIA L, LI S, UMEDA J, TAKAHASHI M, KONDOH K. Length effect of carbon nanotubes on the strengthening mechanisms in metal matrix composites [J]. Acta Materialia, 2017, 140: 317−325.

[10] CHEN B, SHEN J, YE X, IMAI H, UMEDA J, TAKAHASHI M, KONDOH K. Solid-state interfacial reaction and load transfer efficiency in carbon nanotubes (CNTs)-reinforced aluminum matrix composites [J]. Carbon, 2017, 114: 198−208.

[11] ABBASIPOUR B, NIROUMAND B, VAGHEFI S M M, ABEDI M. Tribological behavior of A356−CNT nanocomposites fabricated by various casting techniques [J]. Transactions of Nonferrous Metals Society of China, 2019, 29: 1993−2004.

[12] TOOZANDEHJANI M, OSTOVAN F. Microstructural and mechanical characterization of CNT- and Al_2O_3-reinforced aluminum matrix nanocomposites prepared by powder metallurgy route [J]. Metallography Microstructure and Analysis, 2017, 6: 541−552.

[13] ESAWI A M K, MORSI K. Dispersion of carbon nanotubes (CNTs) in aluminum powder [J]. Composite (Part A): Applied Science and Manufacturing, 2007, 38: 646−650.

[14] SURYANARAYANA C, AL-AQEELI N. Mechanically alloyed nanocomposites [J]. Progress in Materials Science, 2013, 58: 383−502.

[15] OSTOVAN F, MATORI K A, TOOZANDEHJANI M, OSKOUEIAN A, YUSOFF A H M, YUNUS R, ARIFF A H M. Microstructural evaluation of ball-milled nano Al_2O_3 particulate-reinforced aluminum matrix composite powders [J]. International Journal of Materials Research, 2015, 106: 636−640.

[16] TOOZANDEHJANI M, MATORI K A, OSTOVAN F, ABDUL AZIZ S, MAMAT M S. Effect of milling time on the microstructure, physical and mechanical properties of Al−Al_2O_3 nanocomposite synthesized by ball milling and powder metallurgy [J]. Materials, 2017, 10(11): 1232.

[17] OSTOVAN F, MATORI K A, TOOZANDEHJANI M, OSKOUEIAN A, YUSOFF H M, YUNUS R, ARIFF A H M. Nanomechanical behavior of multi-walled carbon nanotubes particulate reinforced aluminum nanocomposites prepared by ball milling [J]. Materials, 2016, 9(3): 140.

[18] OSTOVAN F, MATORI K A, TOOZANDEHJANI M, OSKOUEIAN A, YUSOFF A H M, YUNUS R, ARIFF A H M. QUAH H J, LIM W F. Effects of CNTs content and milling time on mechanical behavior of MWCNT-reinforced aluminum nanocomposites [J]. Materials Chemistry and Physics, 2015, 166:160−166.

[19] ROSELINE S, PARAMASIVAM V. Corrosion behaviour of heat treated aluminium metal matrix composites reinforced with fused zirconia alumina 40 [J]. Journal of Alloys and Compounds, 2019, 799: 205−215.

[20] ASTM B417-13. Standard test method for apparent density of non-free-flowing metal powders using the carney funnel [S]. West Conshohocken: ASTM International, 2006.

[21] ASTM B610-13. Standard test method for measuring dimensional changes associated with processing metal powders [S]. West Conshohocken, PA: ASTM International, 2013.

[22] OLIVER W C, PHARR G M. An improved technique for

determining hardness and elastic modulus using load and displacement sensing indentation experiments [J]. Journal of Materials Research, 1992, 7: 1564−1583.

[23] RAZAVI HESABI Z, HAFIZPOUR H R, SIMCHI A. An investigation on the compressibility of aluminum/nano-alumina composite powder prepared by blending and mechanical milling [J]. Materials Science and Engineering A, 2007, 454−455: 89−98.

[24] GERMAN R M. Sintering theory and practice [M]. New York: Wiley-VCH, 1996.

[25] ASM International Handbook Committee. ASM Handbook: Powder metal technologies and applications [M]. Materials Park, OH: ASM International, 2001.

[26] RAZAVI TOUSI S S, YAZDANI RAD R, SALAHI E, MESBAHPOUR I, RAZAVI M. Production of Al−20wt.% Al_2O_3 composite powder using high energy milling [J]. Powder Technology, 2009, 192: 346−351.

[27] AKBARPOUR M R, SALAHI E, ALIKHANI HESARI F, SIMCHI A, KIM H S. Fabrication, characterization and mechanical properties of hybrid composites of copper using the nanoparticulates of SiC and carbon nanotubes [J]. Materials Science and Engineering A, 2013, 572: 83−90.

[28] LI H, FAN J, GENG X, LI B, LIANG C, WANG H, LI Y, QIAO Z, KANG J. Alumina powder assisted carbon nanotubes reinforced Mg matrix composites [J]. Materials & Design, 2014, 60: 637−642.

[29] KIM H H, BABU J S S, KANG C G. Fabrication of A356 aluminum alloy matrix composite with CNTs/Al_2O_3 hybrid reinforcements [J]. Materials Science and Engineering A, 2013, 573: 92−99.

[30] FATHY A, ABU-OQAIL A, WAGIH A. Improved mechanical and wear properties of hybrid Al−Al_2O_3/GNPs electroless coated Ni nanocomposite [J]. Ceramics International, 2018, 44: 22135−22145.

[31] SAKAI T, BELYAKOV A, KAIBYSHEV R, MIURA H, JONAS J. Dynamic and post-dynamic recrystallization under hot, cold and severe plastic deformation conditions [J]. Progress Materials Science, 2014, 60: 130−207.

[32] LI A B, WANG G S, ZHANG X X, LI Y Q, GAO X, SUN H, QIAN M F, CUI X P, GENG L, FAN G H. Enhanced combination of strength and ductility in ultrafine-grained aluminum composites reinforced with high content intragranular nanoparticles [J]. Materials Science and Engineering A, 2019, 745: 10−19.

[33] SAFARI J, AKBARI G H, SHAHBAZKHAN A, DELSHAD CHERMAHINI M. Microstructural and mechanical properties of Al−Mg/Al_2O_3 nanocomposite prepared by mechanical alloying [J]. Journal of Alloy and Compounds, 2011, 509: 9419−9424.

[34] ZAWRAH M F, ZAYED H A, ESSAWY R A, NASSAR A H, TAHA M A. Preparation by mechanical alloying, characterization and sintering of Cu−20wt.%Al_2O_3 nanocomposites [J]. Materials & Design, 2013, 46: 485−490.

[35] SURYANARAYANA C. Mechanical alloying and milling [J]. Progress Materials Science, 2001, 46: 1−184.

[36] TRINH P V, LUAN N V, PHUONG D D, MINH P N, WEIBEL A, MESGUICH D, LAURENT D. Microstructure, microhardness and thermal expansion of CNT/Al composites prepared by flake powder metallurgy [J]. Composites (Part A): Applied Science and Manufacturing, 2018, 105: 126−137.

[37] KWON H, CHO S, LEPAROUX M, KAWASAKI A. Dual-nanoparticulate reinforced aluminum matrix composite materials [J]. Nanotechnology, 2012, 23: 225704.

[38] TOOZANDEHJANI M, MATORI K A, OSTOVAN F, JAMALUDIN K R, AMRIN A, SHAFIEI E. The effect of the addition of CNTs on the microstructure, densification and mechanical behavior in Al−CNT−Al_2O_3 hybrid nanocomposites [J]. JOM, 2020, 72: 2283−2294.

[39] ZHANG X C, XU B S, XUAN F Z, TU S T, WANG H D, WU Y X. Porosity and effective mechanical properties of plasma-sprayed Ni-based alloy coatings [J]. Applied Surface Science, 2009, 255: 4362−4371.

[40] PRABHU B, SURYANARAYANA C, AN L, VAIDYANATHAN R. Synthesis and characterization of high volume fraction Al−Al_2O_3 nanocomposite powders by high-energy milling [J]. Materials Science and Engineering A, 2006, 425: 192−200.

[41] TOOZANDEHJANI M, MATORI K A, OSTOVAN F, MUSTAPHA F, ZAHARI N I, OSKOUEIAN A. On the correlation between microstructural evolution and ultrasonic properties: A review [J]. Journal of Materials Sciece, 2015, 50: 2643−2665.

[42] SANTHOSH KUMAR S, SESHU BAI V, RAJKUMAR K V, SHARMA G K, JAYAKUMAR T, RAJASEKHARAN T. Elastic modulus of Al−Si/SiC metal matrix composites as a function of volume fraction [J]. Journal of Physics D: Applied Physics, 2009, 42: 175504.

[43] EL-DALY A A, HAMMAD A E. Elastic property and thermal behavior of Sn−Zn based lead-free solder alloys [J]. Journal of Alloy and Compounds, 2010, 505: 793−800.

[44] EL-DALY A A, EL-TANTAWY F, HAMMAD A E, GAAFAR M S, EL-MOSSALAMY E H, AL-GHAMDIE A A. Structural and elastic properties of eutectic Sn−Cu lead-free solder alloy containing small amount of Ag and In [J]. Journal of Alloy and Compounds, 2011, 509: 7238−7246.

[45] EL-DALY A A, ABDELHAMEED M, HASHISH M, DAOUSH W M. Fabrication of silicon carbide reinforced aluminum matrix nanocomposites and characterization of its mechanical properties using non-destructive technique [J]. Materials Science and Engineering A, 2013, 559: 384−393.

[46] EL-DALY A A, ABDELHAMEED M, HASHISH M, EID A M. Synthesis of Al/SiC nanocomposite and evaluation of its mechanical properties using pulse echo overlap method [J]. Journal of Alloy and Compounds, 2012, 542: 51−58.

[47] WU J G, ZHOU S Y, LI X C. Ultrasonic attenuation based inspection method for scale-up production of A206−Al_2O_3 metal matrix nanocomposites [J]. Journal of Manufacturing Science and Engineering, 2015, 137: 011013.

粉末冶金和微波烧结法制备 Al−CNTs−Al_2O_3 纳米复合材料的工艺−显微组织−性能之间的关系

Meysam TOOZANDEHJANI[1], Farhad OSTOVAN[2], Khairur Rijal JAMALUDIN[1], Astuty AMRIN[1], Khamirul Amin MATORI[3], Ehsan SHAFIEI[2]

1. Razak Faculty of Technology and Informatics, Universiti Teknologi Malaysia Kuala Lumpur, 54100 Jalan Semarak, Kuala Lumpur, Malaysia;
2. Department of Material science and Engineering, Islamic Azad University, Bandar Abbas Branch, Bandar Abbas, Hormozgan, Iran;
3. Department of Physics, Faculty of Science, Universiti Putra Malaysia, 43400, Serdang, Selangor, Malaysia

摘　要：采用粉末冶金和微波烧结工艺制备 Al−2CNTs−$x$$Al_2O_3$ 纳米复合材料。研究工艺引起的显微组织特征与材料的物理、力学性能以及超声参数之间的相互关系。研究发现，复合材料的致密化和尺寸变化等物理性能与纳米复合粉体的形貌和粒径密切相关。当 Al_2O_3 含量为 10%(质量分数)、球磨时间大于 8 h、颗粒被大量细化时，材料的密度最大。Al_2O_3 含量、纳米强化相的分布和晶粒尺寸对材料的力学性能有显著影响，当 Al_2O_3 含量为 10%(质量分数)、Al_2O_3 纳米颗粒球磨时间为 12 h、碳纳米管均匀分布时，可形成高密度位错和大量晶粒细化，从而获得最佳的硬度和强度。同时，纵波和横波速度及衰减随着 Al_2O_3 含量和球磨时间的增加而线性增加。超声速度和衰减的变化取决于碳纳米管和 Al_2O_3 在基体中分布的均匀程度及其较小的颗粒间距。经过较长的球磨时间，Al_2O_3 含量越高，碳纳米管和 Al_2O_3 分布越均匀，超声波的速度和衰减越大。

关键词：混杂复合材料；铝基复合材料；粉末冶金；微波烧结；显微组织；力学性能；超声速度；超声衰减

(Edited by Xiang-qun LI)